Available online at www.sciencedirect.com
SCIENCE DIRECT®
Journal of Solid State Chemistry 178 (2005) 1949–1958
JOURNAL OF SOLID STATE CHEMISTRY
www.elsevier.com/locate/jssc

Effect of cation site-disorder on the structure and magneto-transport properties of $Ln_{5/8}M_{3/8}MnO_3$ manganites

J.A. Collado[a], C. Frontera[b], J.L. García-Muñoz[b], M.A.G. Aranda[a,*]

[a]Departamento de Química Inorgánica, Universidad de Málaga, 29071 Málaga, Spain
[b]Instituto de Ciencia de Materiales de Barcelona, CSIC, Campus de Bellaterra, 08193 Bellaterra, Barcelona, Spain

Received 4 March 2005; received in revised form 29 March 2005; accepted 31 March 2005
Available online 26 April 2005

Abstract

Five members of $Ln_{5/8}M_{3/8}MnO_3$ series with A-cation size variance (σ^2) ranging between 3×10^{-4} and 71×10^{-4} Å^2, and the same A-cation size $\langle r_A\rangle = 1.2025$ Å, have been synthesized by the ceramic method. The five manganites are single phase and they crystallize in the *Pnma* perovskite superstructure. The five compositions display ferromagnetic–paramagnetic transitions at temperatures ranging between 130 and 270 K, for the highest and lowest variance sample, respectively. The samples with smaller variances show sharp magnetization transitions and the samples with the larger variances display broad transitions. These transitions have also been studied by differential scanning calorimetry, DSC, and some enthalpy changes are reported. The resistivity study indicates that all samples display the expected metal-to-insulator transitions at temperatures ranging between 140 and 270 K. The samples have been analysed at room temperature by ultra-high-resolution synchrotron powder diffraction and the structural and microstructural features are reported. Furthermore, $Nd_{5/8}Sr_{0.255}Ca_{0.12}MnO_3$ ($\sigma^2 = 40\times10^{-4}$ Å^2) and $Sm_{0.225}Nd_{0.4}Sr_{0.308}Ca_{0.067}MnO_3$ ($\sigma^2 = 53\times10^{-4}$ Å^2) samples have also been studied by synchrotron powder diffraction at 140 K, below the transition temperatures. Both samples are found to be single phase above and below the transition by ultra-high-resolution synchrotron powder diffraction. The microstructure of the samples has been investigated through Williamson–Hall plots. Sample broadenings are markedly anisotropic and strongly dominated by microstrains with average values of the $\Delta d/d$ term close to 14×10^{-4}. A direct correlation is found between the microstrain values and the widths of the magnetization transitions.

Keywords: Manganites; Synchrotron powder diffraction; Conductivity and magnetization characterization

1. Introduction

Electronic and magnetic properties of rare earth manganites, $Ln_{1-x}M_xMnO_3$ (Ln = rare earth, M = alkaline earth), have received a lot of attention in the last decade because of the variety of interesting phenomena exhibited by these materials [1–3]. Besides colossal magnetoresistance CMR, charge ordering, orbital ordering and different types of magnetic ordering, some manganites exhibit phase separation phenomena at different length scales [4]. These systems display a very rich phase diagram. This richness, in crystal structures and physical properties, is due to the subtle competition between charge, orbital, spin and phonon degrees of freedom. Changes in magnetic properties, like ferromagnetic-to-paramagnetic (FM–PM) transition, or electronic properties, like metal-to-insulator (M–I) transition, can be tuned in several ways.

The main way to vary the physical properties of manganites is to control the charge carriers concentration. In early studies, the changes in electronic properties were mainly described by changing the doping level x, which for a given oxygen content defines the Mn^{3+}/Mn^{4+} ratio and, so, the charge carriers concentration. Archetypal examples of this type of studies are the

*Corresponding author. Fax: +34 952 132 000.
E-mail address: g_aranda@uma.es (M.A.G. Aranda).

0022-4596/$ - see front matter © 2005 Elsevier Inc. All rights reserved.
doi:10.1016/j.jssc.2005.03.046

$La_{1-x}Sr_xMnO_3$ [5–8] and $La_{1-x}Ca_xMnO_3$ [9,10] series. A second mechanism allows to change the magnetic and electronic properties, for fixed x values, by varying the average A-cation radii, where A stands for the large lanthanide/alkaline-earth site. Thus, the behaviours of series like $La_{5/8-y}Pr_yCa_{3/8}MnO_3$, $La_{0.70-y}Pr_yCa_{0.30}MnO_3$, and $Nd_{0.7}Sr_{0.3-y}Ca_yMnO_3$ have been widely studied [11–20]. The variation in the properties of these series has been parameterized through the changes in the average cation radius $\langle r_A\rangle$. The variation of this parameter induces a tilting in the Mn–O–Mn angles that modifies the bandwidth. A third mechanism, for fixed x and $\langle r_A\rangle$ values, allows to finely change the magneto-transport properties by inducing A-site cation disorder which is due to the disparity or mismatch of individual A-cation radii [21]. There are several examples of these series, and the change in the properties has been parameterized using the A-cation size variance, $\sigma^2(=\langle r_A^2\rangle - \langle r_A\rangle^2)$ [22]. For instance, the series $Ln_{0.70}M_{0.30}MnO_3$ has been deeply studied [23,24].

Regarding the second mechanism, an archetypal series is $La_{5/8-y}Pr_yCa_{3/8}MnO_3$ [11,12] which displays a very rich phase diagram at low temperatures, including phase separation. The doping level is constant, $x = 3/8$, and it is chosen because the Curie temperature, T_c, is maximized at this charge carrier concentration in the $La_{1-x}Ca_xMnO_3$ system. $\langle r_A\rangle$ changes along the series from 1.2025 Å for $y = 0$ to 1.1785 Å for $y = 5/8$. Finally, the A-size variance is very small and it goes from $\sigma^2 \times 104 = 3$ Å^2 to $\sigma^2 \times 10^4 = 0$, for $y = 0$ and $y = 5/8$ samples, respectively. This series displays metallic properties ($y = 0$) and semiconducting behaviour ($y = 5/8$) at low temperatures. Furthermore, for the midway sample ($y = 0.35$, $\langle r_A\rangle = 1.190$ Å), a M–I transition with CMR and mesoscopic phase separation [11] at low temperature has been reported [11,13,14]. Below 200 K, ferromagnetic-metal, antiferromagnetic-semiconducting-charge-ordered, and even antiferromagnetic-semiconducting-charge-disordered phases have been proposed to coexist [13,14].

Regarding the third mechanism, an archetypal series is $Ln_{0.70}M_{0.30}MnO_3$ [23,24]. The Curie (and M–I) transition shows a strong negative correlation with σ^2 (for fixed values of $x = 0.30$ and $\langle r_A\rangle = 1.20$ Å). All samples have the orthorhombic *Pnma* superstructure but the lattice strain in the *ac* plane [$S_{ac} = 2(c-a)/(c+a)$] changed from +0.3% to −0.03% going from the orbital disordered (low σ^2) to the orbital ordered (high σ^2) samples [24]. In this series, phase coexistence at low temperature was not detected by high-resolution synchrotron powder diffraction [23] but subsequent ESR and magnetization studies revealed a broad co-existence region [24].

This work is part of an on-going research devoted to progress in the understanding of the origin of the low-temperature mesoscopic phase separation displayed by some manganites. We have previously reported the room-temperature (RT) synchrotron powder diffraction data and magneto-transport properties for $La_{5/8-y}Pr_yCa_{3/8}MnO_3$ samples [12], and low-temperature synchrotron powder diffraction show mesoscopic phase separation for some compositions [25]. In this paper, we report the influence of A-cation size variance in $Ln_{5/8}M_{3/8}MnO_3$, where the doping level ($x = 3/8$) and A-cation radii ($\langle r_A\rangle = 1.2025$ Å) are kept constant. We report the room and low temperatures structures, and the magneto-transport properties. An important finding of this study is the absence of mesoscopic phase separation below the transition temperatures due to the A-site cation disorder in these chemically complex samples.

2. Experimental

2.1. Synthesis

The five compositions shown in Table 1 were chosen to have a constant mean radius, ($\langle r_A\rangle = 1.2025$ Å), but the A-cation size variance changes. The variance values were calculated using standard nine-coordinated cation radii [26] as in previous works [21–24]. $La_{5/8}Ca_{3/8}MnO_3$ ($\sigma^2 \times 10^4 = 3$ Å^2), $Pr_{5/8}Sr_{0.178}Ca_{0.197}MnO_3$ ($\sigma^2 \times 10^4 = 25$ Å^2), $Nd_{5/8}Sr_{0.255}Ca_{0.12}MnO_3$ ($\sigma^2 \times 10^4 = 40$ Å^2), $Sm_{0.225}Nd_{0.4}Sr_{0.308}Ca_{0.067}MnO_3$ ($\sigma^2 \times 10^4 = 53$ Å^2) and $Sm_{0.504}Nd_{0.121}Sr_{3/8}MnO_3$ ($\sigma^2 \times 10^4 = 71$ Å^2) were prepared by the ceramic method using high-purity oxides/carbonates and are hereafter labelled as 3, 25, 40, 53, 71, respectively. Oxides were pre-calcined at 1000 °C for 2 h in order to achieve decarbonation. Several thermal and grinding treatments were carried out to ensure the highest possible chemical homogeneity. Firstly, stoichiometric amounts of the oxides and carbonates (calculated to obtain ten grams of each manganite) were thoroughly mixed in an agate mortar and heated at 950 °C for 12 h. Secondly, the powdered sample was placed in a Fritsch ball mill (model Pulverisette 7, agate balls and container) and isobutyl alcohol was added, approx. 6 mL, which acts as homogenizing agent. The overall time in the ball mill was 4 h at 100 rpm. The spinning direction was switched each 20 min to optimize grinding. The "wet" mixture was heated at 100 °C to remove the remaining alcohol and heated again at 950 °C for another 12 h. Thirdly, the powder was again ball milled and dried as indicated above. The mixture was pelletized at 150 MPa, and heated at 1450 °C for 12 h. Finally, the pellets were grounded in an agate mortar, pelletized and sintered at 1500 °C for another 12 h. All heating rates were

Table 1
Summary of chemical, structural and physical data for the $Ln_{5/8}M_{3/8}MnO_3$ series

A-Composition	σ^2 (Å^2)	T_c[a] (K)	ΔT_c[b] (K)	T_c[c] (K)	T_{MI}[d] (K)	*a* (Å)	*b* (Å)	*c* (Å)	S_{ac}
$La_{5/8}Ca_{3/8}$	3×10^{-4}	269.1(1)	5.7(4)	271	270	5.44781(3)	7.69370(4)	5.46164(3)	0.25
$Pr_{5/8}Sr_{0.178}Ca_{0.197}$	25×10^{-4}	236.9(1)	7.4(3)	235	238	5.44231(3)	7.68862(3)	5.45267(2)	0.19
$Nd_{5/8}Sr_{0.255}Ca_{0.12}$	40×10^{-4}	197.6(1)	6.9(4)	197	201	5.44516(2)	7.68826(2)	5.44649(2)	0.02
$Nd_{5/8}Sr_{0.255}Ca_{0.12}$[e]	40×10^{-4}					5.43724(2)	7.67730(2)	5.43771(2)	0.02
$Sm_{0.225}Nd_{0.4}Sr_{0.308}Ca_{0.067}$	53×10^{-4}	189.9(2)	38.1(9)	—	189	5.44317(4)	7.68591(5)	5.44867(5)	0.10
$Sm_{0.225}Nd_{0.4}Sr_{0.308}Ca_{0.067}$[e]	53×10^{-4}					5.43533(5)	7.67541(6)	5.43971(2)	0.08
$Sm_{0.504}Nd_{0.121}Sr_{3/8}$	71×10^{-4}	129.9(1)	26.0(6)	—	139	5.44695(4)	7.68555(4)	5.44505(3)	−0.03

[a]Curie transition temperature from the magnetization study on heating determined from a Lorentzian function fit of the derivative curves.
[b]Width of the magnetization transition.
[c]Transition temperature from the DSC study on heating.
[d]MI transition temperature from the resistivity study on heating.
[e]Structural data at 140(2) K.

10 °C/min and all cooling rates were those obtained by turning off the furnace.

2.2. Powder diffraction

All samples were characterized by Laboratory X-ray Powder Diffraction at room temperature to check the phase purity. Full structural characterization was carried out by ultra-high-resolution Synchrotron X-ray Powder Diffraction, SXRPD. The SXRPD patterns were collected on ID31 powder diffractometer at ESRF, Grenoble. The samples were loaded in a borosilicate glass capillary ($\phi = 0.5$ mm) and rotated during data collection. A short penetrating wavelength, $\lambda = 0.400269$ Å (30.97 keV), was selected with a double-crystal Si(111) monochromator and calibrated with Si NIST ($a = 5.43094$ Å). The RT runs took about 1 h to have good statistics over the angular range 3–40° in 2θ (Q ranging between 1 and 9 Å^{-1}). Two low-temperature patterns, $T = 140(2)$ K, for $\sigma^2\times10^4 = 40$ and $\sigma^2\times10^4 = 53$ samples were collected using a continuous liquid-helium flow cryostat with spinning capillary. The data from the multi-analyser stage coupled with the nine detectors were normalized and summed into 0.003° step size with local software to produce the final raw data. The instrumental full-width at half-maximum, FWHM, in the operating conditions was determined by recording a room temperature pattern for $Na_2Al_2Ca_3F_{14}$, NAC, as previously described [12]. This compound shows the narrowest diffraction peaks with FWHM values approaching to those theoretically calculated for this ultra-high-resolution diffractometer.

2.3. Magnetic and transport study

Magnetization and resistivity data were recorded in a Quantum Design PPMS (Physical Properties Measurement System). DC magnetization data have been collected with an applied field of 0.1 T on heating from 5 to 300 K (field cooled). Resistivity data were measured in zero field using the standard four probe method on a cooling–warming cycle at 3 K/min rate.

2.4. Calorimetric study

The calorimetric data have been obtained using differential scanning calorimetry, DSC, with computer-aided data analysis (Shimadzu DSC-50). The studied temperature range was from 300 to 160 K and the scanning rate was 5 K/min^{-1}.

3. Results

3.1. Magnetization study

The five studied samples show a FM–PM transition in the magnetization data, see Fig. 1. The transitions in 3, 25 and 40 samples are sharp but those in 53 and 71 samples are very broad. This can be better seen, and quantified, in Fig. 2 where the derivatives of the magnetization/field ($d(M/H)/dT$) data for the five samples are shown. The peaks in the derivative curves have been fitted with a Gaussian and a Lorentzian function to obtain the T_c values and the transition widths (FWHM), ΔT_c. The fits are invariably better with the Lorentzian function and the results, T_c and ΔT_c, using these fits are given in Table 1. The variation of T_c with σ^2 is displayed in Fig. 3 where a linear behaviour is observed. The rate of suppression of T_c with σ^2 (the slope of Fig. 3, $dT_c/d\sigma^2$) is approximately 2×10^4 K Å^{-2}.

3.2. Calorimetric study

Fig. 4 shows the raw DSC data for the five samples on heating. The curves for the first three samples, 3, 25, 40,

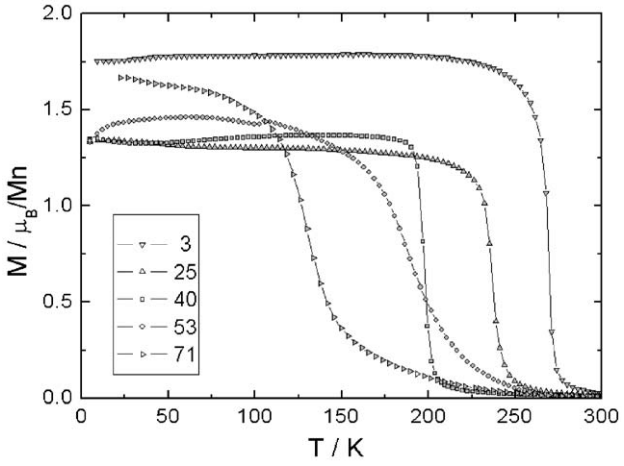

Fig. 1. Magnetization versus temperature curves, on heating, for the $Ln_{5/8}M_{3/8}MnO_3$ series (cooled under 0.1 T field). The $\sigma^2 \times 10^4/\text{Å}^2$ values are labelled.

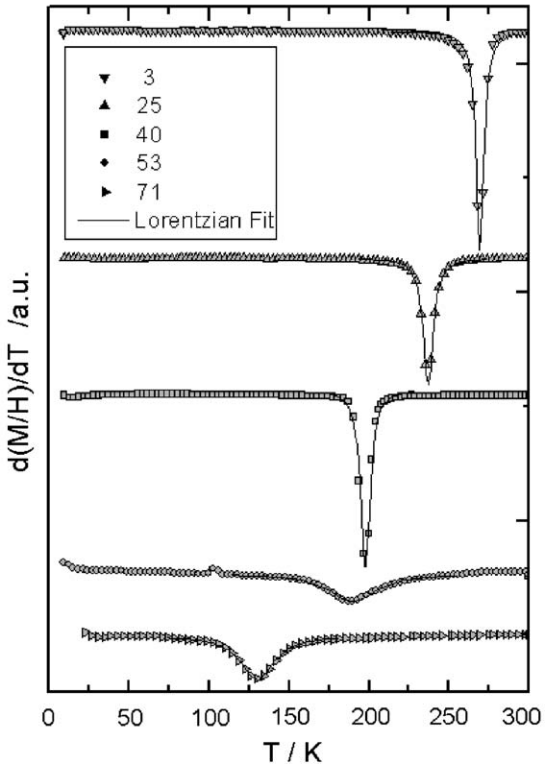

Fig. 2. Derivatives of the magnetization/field ($d(M/H)/dT$) for the five samples. The $\sigma^2 \times 10^4/\text{Å}^2$ values are labelled and the Lorentzian fit to the peaks is also shown.

show a clear transition (endotherm on heating) and the temperatures of these peaks are also given in Table 1. The 53 and 71 samples do not show a transition in the explored temperature range (160–300 K). The integrated area of the DSC peaks gives the enthalpy changes in the transitions and they are 440, 304 and 387 J/mol for 3, 25, 40 samples, respectively.

3.3. Resistivity study

The resistivity curves for the five samples are displayed in Fig. 5. It is observed that all the samples undergo low temperature M–I transitions. The transition temperatures, T_{MI}, were taken from the maxima on heating and they are given in Table 1.

3.4. Structural study

The five manganites are single phase and crystallize in the orthorhombic *Pnma* perovskite superstructure. Good structural descriptions have been obtained for all the compositions at RT from Rietveld refinement of SXRPD using the GSAS suite of programs [27]. The methodology and details of the fits to the synchrotron powder data are the same as previously reported [12]. The 140 K patterns of the 40 and 53 samples were also *Pnma* single phase by ultra-high-resolution SXRPD. Final unit cell parameters are given in Table 1. The lattice strain values in the *ac* plane (S_{ac}, determined as described in the introduction section) are also given in Table 1. The Rietveld disagreement factors, positional and thermal atomic parameters are given in Table 2. The Mn–O bond distances, Mn–O–Mn bonding angles are also given in Table 2. As an example of the good quality of the fits, the RT Rietveld plot for the $\sigma^2 \times 10^4 = 40$ sample is given in Fig. 6.

3.5. Microstructural study

Details about the microstructures of the series can be obtained from the Williamson–Hall plots [28], which have been previously applied to manganites [12,29,30]. Williamson–Hall plots relate the mean coherent diffraction domains [L (Å)] and the distribution of d-spacings [$\Delta d/d$] for a selected class of reflections through the equation $\text{FWHM}\cos(\theta) = (K\lambda/L) + 2(\Delta d/d)\sin(\theta)$, where FWHM is expressed in radians and must be corrected from the diffractometer contribution ($0.002^\circ/2\theta$, determined from the pattern of NAC), K is a shape factor close to unity, λ is the wavelength of the experiment, L is the mean coherent diffraction domain size (for a class of reflections) and $\Delta d/d$ is the sample broadening factor due to the microstrains (for a class of reflections). We have carried out the Williamson–Hall plots for several classes of reflections along the series. The values of $K\lambda/L$ terms (ordinate at the origin) are very small (all the values are between 2×10^{-5} and 12×10^{-5}). The obtained $\Delta d/d$ values are given in Table 3.

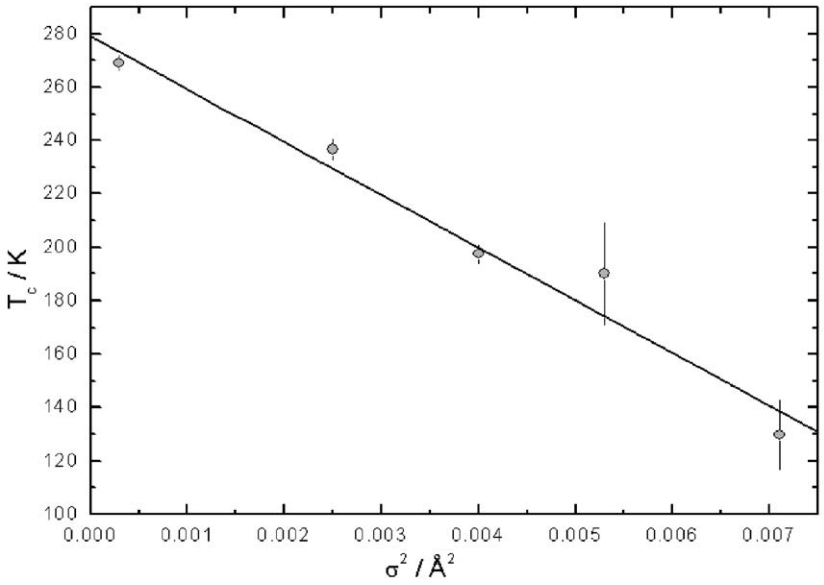

Fig. 3. T_c, obtained from the fits of one lorentzian function to the $d(M/H)/dT$ data, versus σ^2. The full error bars correspond to the width of the transition determined as described in the text.

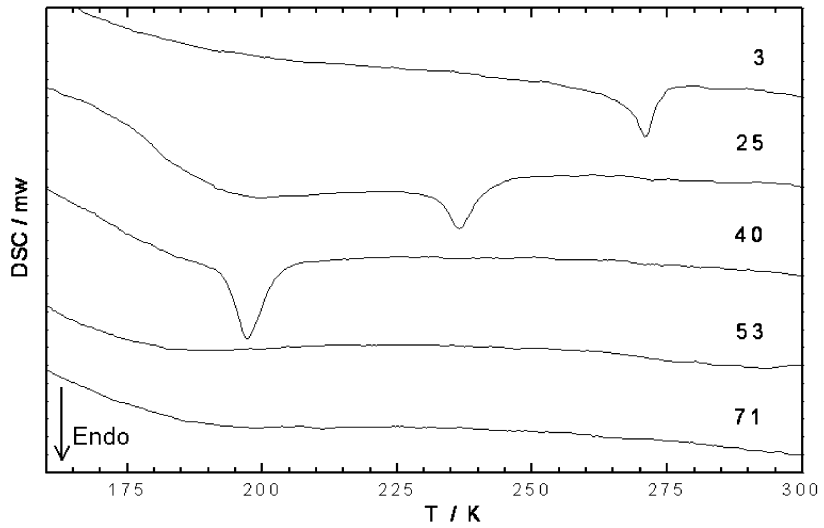

Fig. 4. DSC versus temperature curves, on heating, for the $Ln_{5/8}M_{3/8}MnO_3$ series. The $\sigma^2 \times 10^4/\text{Å}^2$ values are labelled.

4. Discussion

4.1. Magnetization study

The magnetization data given in Figs. 1 and 2 show a unique transition that broadens with increasing σ^2. This result is consistent with full series being orbital disordered (no evidence of antiferromagnetic anomalies from possible minority orbital order or charge-order regions was detected for all the σ^2 values). The broadening of the transition with σ^2 has been very recently reported [24] for $Ln_{0.70}M_{0.30}MnO_3$ and some compositions showed the coexistence of two phases (orbital disordered and orbital ordered). The two phases were easily detected from $M(T)$ data because two separated peaks were apparent in the derivatives of the magnetization/field ($d(M/H)/dT$) curves. The samples reported here do show a unique peak which points to a mesoscopic single phase behaviour with temperature. The variation of T_c with σ^2 (see Fig. 3) is linear within the errors and the obtained rate of suppression, $dT_c/d\sigma^2 \sim 2 \times 10^4\,\text{K}\,\text{Å}^{-2}$, is larger than that obtained for $Ln_{0.70}M_{0.30}MnO_3$ $\sim 1 \times 10^4\,\text{K}\,\text{Å}^{-2}$ [24].

4.2. Calorimetric study

DSC curves, Fig. 4, exhibit well-defined endothermic peaks (similar to those previously described

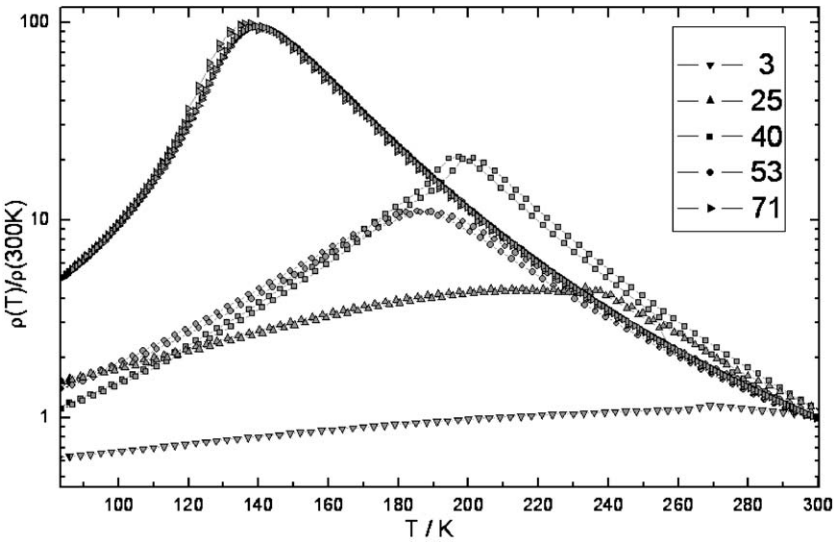

Fig. 5. Resistivity, RT-normalized, versus temperature curves (cooling and heating cycle) for the $Ln_{5/8}M_{3/8}MnO_3$ series. The $\sigma^2 \times 10^4/\text{Å}^2$ values are labelled.

Table 2
Rietveld disagreement factors, refined atomic parameters, and selected bond distances and angles for the $Ln_{5/8}M_{3/8}MnO_3$ series

	3	25	40	40 (140 K)	53	53 (140 K)	71
R_{WP} (%)	8.41	6.73	6.21	8.32	6.84	9.43	5.55
R_P (%)	6.30	4.81	4.64	5.39	4.76	6.70	3.73
R_F (%)	3.44	4.81	3.41	3.92	3.64	3.96	1.86
A, 4, ($x\frac{1}{4}z$)							
x	0.0188(1)	0.0233(1)	0.0263(1)	0.0270(1)	0.0254(1)	0.0257(1)	0.0271(1)
z	−0.0033(1)	−0.0040(1)	−0.0048(1)	−0.0051(1)	−0.0046(1)	−0.0046(2)	−0.0049(1)
Uiso × 100 Å^2	0.95(1)	0.82(1)	0.91(1)	0.45(1)	0.82(1)	0.43(1)	0.87(1)
Mn, 4 ($00\frac{1}{2}$)							
Uiso × 100 Å^2	0.59(2)	0.36(1)	0.71(1)	0.09(1)	0.57(1)	0.25(1)	0.56(1)
O1, 4c ($x\frac{1}{4}z$)							
x	−0.0078(2)	−0.0062(4)	−0.0065(4)	−0.0077(5)	−0.0055(4)	−0.0079(7)	−0.0053(4)
z	0.4386(2)	0.4354(6)	0.4337(6)	0.4347(7)	0.4347(8)	0.4324(12)	0.4338(7)
Uiso × 100 Å^2	1.1(1)	0.9(1)	1.4(1)	1.0(1)	1.1(1)	0.7(2)	1.5(1)
O2, 8d (xyz)							
x	0.7236(1)	0.7221(5)	0.7201(5)	0.7181(6)	0.7213(6)	0.7237(9)	0.0721(1)
y	−0.0322(1)	−0.0329(3)	−0.336(2)	−0.0341(3)	−0.0337(3)	−0.0334(6)	−0.0333(3)
z	0.2756(1)	0.278(4)	0.2779(5)	0.2785(6)	0.2771(6)	0.2775(9)	0.2771(5)
Uiso × 100 Å^2	1.1(1)	1.0(1)	1.5(1)	1.1(1)	1.4(1)	0.7(1)	1.5(1)
Mn–O1 × 2/Å	1.953(1)	1.954(1)	1.956(1)	1.952(1)	1.954(1)	1.954(1)	1.955(1)
Mn–O2 × 2/Å	1.957(2)	1.955(3)	1.963(3)	1.967(4)	1.956(4)	1.955(6)	1.963(4)
Mn–O2 × 2/Å	1.952(2)	1.954(3)	1.948(3)	1.941(4)	1.949(4)	1.946(6)	1.945(4)
Mn–O1–Mn (deg)	160.1(1)	159.1(2)	158.6(2)	158.9(2)	159.0(2)	158.2(4)	158.7(2)
Mn–O2–Mn (deg)	161.2(1)	160.5(1)	159.9(1)	159.3(1)	160.2(1)	160.6(2)	160.2(1)

for $La_{1-x}Ca_xMnO_3$ [31], that showed first-order-type transitions). The temperatures of the transitions obtained from the DSC study agree very well with those obtained from the magnetization study, see Table 1. Besides the magnetic degrees of freedom, the heat transfer also accounts for the entropy and lattice energy gain due to the electronic delocalization. Namely, local lattice structural changes from the delocalization of the polaronic charge carriers are also contributing to the observed endothermic peaks. We note that the endothermic phase transition was only observed for $\sigma^2 \times 10^4 = 3$, 25 and 40 samples. Not such a transition could be observed in 53 and 71 samples. Several measurements were carried out at different experimental conditions and with samples from different synthetic batches. The absence of the DSC peak is reproducible

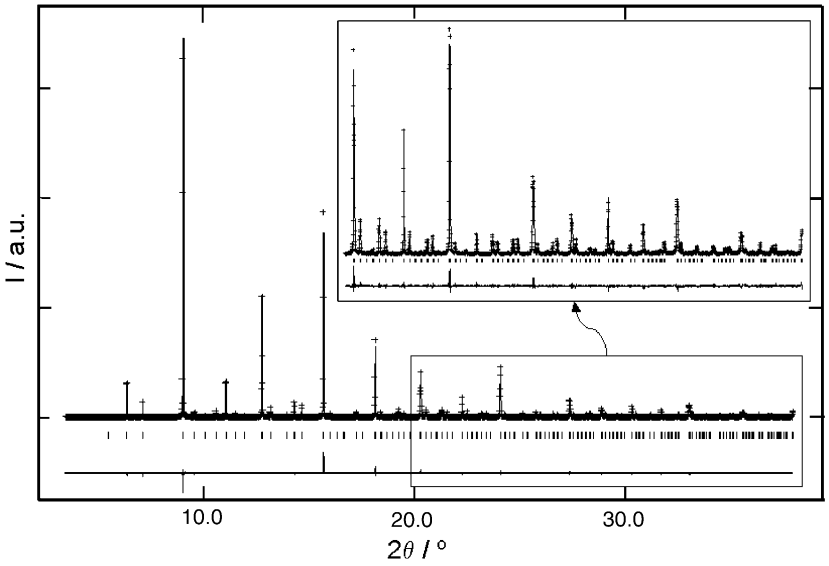

Fig. 6. Observed (crosses), calculated (full line) and difference (bottom) SXRPD pattern for $Nd_{5/8}Sr_{0.255}Ca_{0.12}MnO_3$ ($\sigma^2 \times 10^4 = 40$) at room temperature. The inset shows an enlarged view of the high-angle region.

Table 3
Selected microstructural data at room temperature for the $Ln_{5/8}M_{3/8}MnO_3$ series from SXRPD data by using the Williamson–Hall representations

	3	25	40	53	71
$\Delta d/d \times 10^4$ (020)[a]	12(1)	13(1)	11(1)	19(1)	21(1)
$\Delta d/d \times 10^4$ (202)[b]	11(1)	13(1)	11(1)	19(1)	21(1)
$\Delta d/d \times 10^4$ (022)[c]	8	5	5	17	22
$\Delta d/d \times 10^4$ (220)[d]	8	8	8	17	14

[a]Reflections used: (020), (040), (080).
[b]Reflections used: (101), (202), (404).
[c]Only two reflections used: (022), (044) because the remaining peaks are very weak, so, errors cannot be given.
[d]Only two reflections used: (220), (440), because the systematic absences, so errors cannot be given.

for the last two compositions. One could speculate that the sample with $\sigma^2 \times 10^4 = 71$ did not display the transition in the DSC curve because it should take place close to 130–140 K out of our measurable temperature range. However, the FM–PM transition for $\sigma^2 \times 10^4 = 53$ sample should take place close to 180 K but it is not present, see Fig. 4. Very likely, the transition is not evident, in the DSC curve, because it is spread over a very large temperature range. In the highest variance sample, the broad transition observed in $M(T)$ and $\rho(T)$ curves indicates that the coexistence of collinear ferromagnetic and non-ferromagnetic regions extends over more than 75 K. Proving that in high variance samples the transition shown by the resistivity at the region of greatest slope in $M(T)$ is percolative in nature. Consequently, in such a case, local lattice changes associated with charge delocalization over very small finite regions should occur spread out along a wide temperature range, thus leading to the disappearance of the well-defined sharp endothermic peak.

The difference in the Gibbs free energy ($\Delta G = \Delta H - T\Delta S$) of the phases at both sides of the transition vanishes at the transition point ($\Delta G = 0$), where $\Delta S = \Delta H/T$. The observed endotherms ($\Delta H > 0$) indicate that the disorder increases along the transition on heating, as expected. The total entropy change values are calculated to be 1.62, 1.29 and 1.96 J/K mol for 3, 25, 40 samples, respectively (similar to the values found in $La_{1-x}Ca_xMnO_3$ [31]). It is known that in these ferromagnetic metallic phases, the total entropy change is very different to the spin entropy change coming from the order/disorder moment transition [32]. Moreover, the measured values of the enthalpy change (440, 304 and 387 J/mol for 3, 25, 40 samples, respectively) seem to depend on different terms with dependence on the transition temperature, microstructural lattice strains, etc.

4.3. Resistivity study

The resistivity curves, Fig. 5, show a MI transition on heating in all the samples which takes place at temperatures very close to those of the FM–PM transitions, see Table 1. The variation of the values of the resistivity is relatively small (lower than two orders of magnitude) along the series, see Fig. 5. This is another significant difference, when the behaviour of this series and that of the $Ln_{0.70}M_{0.30}MnO_3$ series are compared [23]. The reason is that the resistivity values for the orbital ordered samples are much larger (more than 3 orders of magnitude) than those of the orbital disordered samples. Thus, the electrical behaviour along the $Ln_{5/8}M_{3/8}MnO_3$ series is fully compatible with all samples being orbital disordered with relatively similar resistivities.

4.4. Structural study

All the samples are single highly crystalline phases by ultra-high-resolution SXRPD and they crystallize in the *Pnma* superstructure. The unit cell parameters and the lattice strain values in the *ac* plane, S_{ac}, given in Table 1, agree with the five compositions being orbital disordered at room temperature. The magnetic and transport properties are consistent with this finding as all samples have relatively low resistivities and no other anomalies in $M(T)$ than a unique FM–PM transition. In the $Ln_{0.70}M_{0.30}MnO_3$ series with $\langle r_A\rangle = 1.20$ Å, the borderline for a change between the orbital disordered and orbital ordered phases was found very close to $a = c$ (and so, $S_{ac} = 0$). In the present case, however, the $\sigma^2 \times 10^4 = 71$ sample has $S_{ac} = -0.03\%$ but its magnetic and transport properties correspond to those of the orbital disordered phases. The Mn–O bond distances and angles in Table 2 have the expected values and confirm the same average structural distortion for all the investigated samples.

A key point is to know if these compounds are single phase by ultra-high-resolution SXRPD on cooling across the transition. Low-temperature mesoscopic phase separation for similar compositions, but with slightly lower average *A*-cation size (for instance $La_{5/8-y}Pr_yCa_{3/8}MnO_3$, with $y = 0.35$ and so, $\langle r_A\rangle = 1.190$ Å) has been reported by electron microscopy [11] and we can confirm this by ultra-high-resolution SXRPD [25]. We have checked the low-temperature phase behaviour for two samples, $Nd_{5/8}Sr_{0.255}Ca_{0.12}MnO_3$ ($\sigma^2 \times 10^4 = 40$ Å^2) and $Sm_{0.225}Nd_{0.4}Sr_{0.308}Ca_{0.067}MnO_3$ ($\sigma^2 \times 10^4 = 53$ Å^2), which are representative of the two types of magnetization curves, sharp and broad transitions, respectively. The SXRPD data at 140 K show that these compounds are single phase without extra peaks due to charge/orbital ordering similar to those of

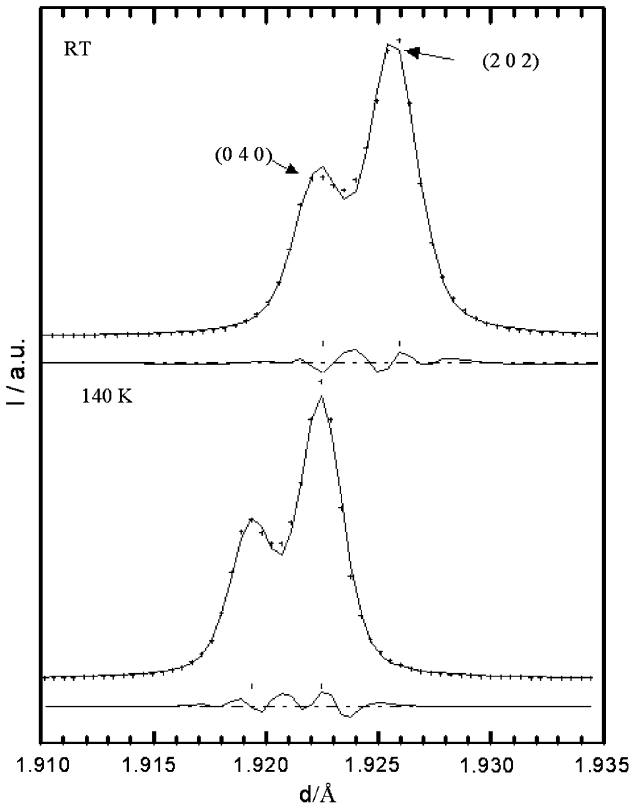

Fig. 7. Selected key region (1.910−1.935 Å) of the fitted SXRPD patterns (RT top; 140 K bottom) for $Nd_{5/8}Sr_{0.255}Ca_{0.12}MnO_3$ ($\sigma^2 \times 10^4 = 40$) sample. The two Bragg peaks (202) and (040) are labelled.

$Pr_{0.60}Ca_{0.40}MnO_3$ [33] and $Pr_{5/8}Ca_{3/8}MnO_3$ [25]. Figs. 7 and 8 display a selected key region containing the (202) and (040) Bragg peaks at temperatures above and below the transition. This is the most sensitive part of the powder pattern to phase separation, as if there are two cells with different *c*-values, this can be seen as a new shoulder at low temperature [25]. Furthermore, if a low-temperature orbital ordered phase appears, similar to that of monoclinic $Pr_{0.60}Ca_{0.40}MnO_3$ [33], then a new extra reflection $(20\bar{2})$ should develop. The low-temperature patterns of 40 and 53 samples do not show any characteristic of phase separation although they are chemically quite complex with four cations in the *A*-site for the last sample.

4.5. Microstructural study

The microstructure of the samples have been analysed by the Williamson–Hall methodology and the $\Delta d/d$ sample broadening factor due to the microstrains (for a given class of reflections), are presented in Table 3. This term includes the effects of structural defects such as dislocations, stacking faults, twin boundaries, intergrowths, etc. For solid solutions, the $\Delta d/d$ term also has

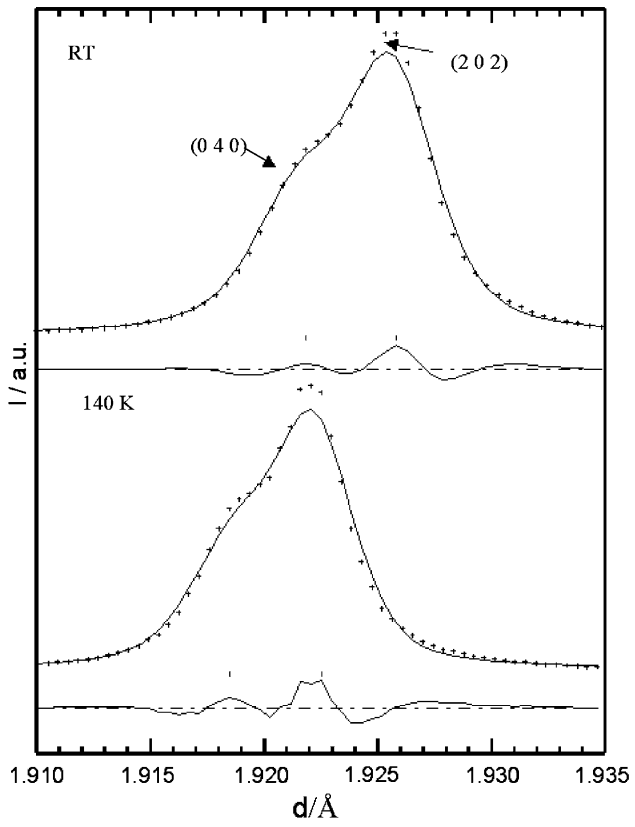

Fig. 8. Selected key region (1.910–1.935 Å) of the fitted SXRPD patterns (RT top; 140 K bottom) for $Sm_{0.255}Nd_{0.4}Sr_{0.308}Ca_{0.067}$ ($\sigma^2 \times 10^4 = 53$) sample. The two diagnostic Bragg peaks (202) and (040) are labelled.

a main contribution from the chemical quality of the sample since a larger distribution of the unit cell values due to possible chemical heterogeneity results in broader peaks. Hence, it is possible to assess the overall quality of the sample by obtaining the $\Delta d/d$ values. Numbers larger than 10^{-3} are typical of manganites with many defects and numbers lower than 5×10^{-4} are typical of manganites with very few defects and very good chemical homogeneity [12,29,30]. The results shown in Table 3 indicated that the broadening is due to microstrains and that the contribution of the coherent diffraction domain sizes to the FWHMs are almost negligible. The values of the $K\lambda/L$ terms are small (between 2×10^{-5} and 12×10^{-5}) and hence, the coherent diffraction domain sizes must be larger than 3000 Å.

The sample broadening due to microstrains is variable, with the $\Delta d/d$ term ranging between 5 and 22×10^{-4}, see Table 3. Three main conclusions can be drawn from this microstructural study. Firstly, and as an expected general trend, the samples with smaller *A*-cation variance show smaller microstrain values. Secondly, there is a clear correlation between the microstrain values, Table 3, and the width of the magnetization transitions, Table 1. The $\sigma^2 \times 10^4 = 40$ and 3 $Å^2$ samples show the smaller microstrain values and the sharper magnetization transitions. Conversely, the $\sigma^2 \times 10^4 = 53$ and 71 $Å^2$ samples show the larger microstrains and the broader transitions. It is worthy to note that the $Nd_{5/8}Sr_{0.255}Ca_{0.12}MnO_3$ ($\sigma^2 \times 10^4 = 40$) sample shows very narrow diffraction peaks and a very sharp magnetization transition. Thirdly, the sample broadening is markedly anisotropic, see Table 3, which points to structural defects as the main origin, with the cation inhomogeneity (likely isotropic) playing a much less important role. $Nd_{5/8}Sr_{0.255}Ca_{0.12}MnO_3$ sample, with three cations in the *A*-site, has slightly smaller microstrain values than $La_{5/8}Ca_{3/8}MnO_3$ and $Pr_{5/8}Ca_{3/8}MnO_3$ [12], which have only two cations in the *A*-site.

5. Conclusions

$Ln_{5/8}M_{3/8}MnO_3$ series, with variable *A*-cation size variance (3×10^{-4} $Å^2 \leqslant \sigma^2 \leqslant 71 \times 10^{-4}$ $Å^2$), crystallizes in the orthorhombic *Pnma* perovskite superstructure. The synchrotron data above and below the ferromagnetic-to-paramagnetic (and so, metal-to-insulator) transition do not show any sign of phase separation at low temperatures. The magneto-transport properties are typical of single phase manganites with orbital disordered structures. The samples with smaller variances show sharp magnetization transitions and those with the larger variances display broad transitions. The powder diffraction peak broadening, analysed by the Williamson–Hall methodology, is markedly anisotropic and strongly dominated by microstrains likely due to structural defects. There is a clear correlation between the microstrain values and the widths of the magnetization transitions.

Acknowledgments

Financial support from the CICyT MAT2003-7483-C2 research grant is acknowledged. C.F. acknowledges financial support from MEC (Spanish government). ESRF is thanked for the provision of X-ray synchrotron powder diffraction facility.

References

[1] C.N.R. Rao, B. Raveau (Eds.), Colossal Magnetoresistance, Charge Ordering and Related Properties of Manganese Oxides, World Scientific, Singapore, 1998.
[2] Y. Tokura (Ed.), Colossal Magnetoresistive Oxides, Gordon & Breach Sience, New York, 2000.
[3] S. Jin, T.H. Tiefel, M. McCormack, R.A. Fastnacht, L. Schultz, K. Samwer, Science 264 (1994) 413.

[4] E. Dagatto, T. Hotta, A. Moreo, Phys. Rep. 1 (2001) 344; N.D. Mathur, P.B. Littlewood, Solid State Commun. 119 (2001) 271.
[5] A. Moreo, S. Yunoki, E. Dagotto, Science 283 (1999) 2034.
[6] A. Moreo, M. Mair, A. Feiguin, S. Yunoki, E. Dagotto, Phys. Rev. Lett. 84 (2000) 5568.
[7] A. Urushibara, Y. Moritomo, T. Arima, A. Asamitsu, G. Kido, Y. Tokura, Phys. Rev. B 51 (1995) 103.
[8] Y. Moritomo, T. Akimoto, A. Nakamura, K. Ohayama, M. Ohashi, Phys. Rev. B 58 (1998) 5544.
[9] G.H. Jonker, J.H. Van Santen, Physica (Utrech) 16 (1950) 337.
[10] P. Schiffer, A.P. Ramirez, W. Bao, S.W. Cheong, Phys. Rev. Lett. 75 (1995) 3336.
[11] M. Uehara, S. Mori, C.H. Chen, S.W. Cheong, Nature 399 (1999) 560.
[12] J.A. Collado, C. Frontera, J.L. García-Muñoz, C. Ritter, M. Brunelli, M.A.G. Aranda, Chem. Mater. 15 (2003) 167.
[13] K.H. Kim, M. Uehara, C. Hess, P.A. Sharma, Phys. Rev. Lett. 84 (2000) 2961.
[14] V. Kiryukhin, B.G. Kim, S.W. Cheong, T.Y. Hoo, J.P. Hill, I. Moon, Y.H. Jeong, Phys. Rev. B 63 (2000) 024420.
[15] H.Y. Hwang, S.W. Cheong, P.G. Radaelli, M. Marezio, B. Batlogg, Phys. Rev. Lett. 75 (1995) 914.
[16] F. Millange, V. Caignaert, G. Mather, E. Suard, B. Raveau, J. Solid State Chem. 127 (1996) 131.
[17] V. Caignaert, E. Suard, S. Maignan, C.H. Simon, B. Raveau, J. Magn. Magn. Mater. 153 (1996) L260.
[18] P.G. Radaelli, G. Iannone, M. Marezio, H.Y. Hwang, S.W. Cheong, J.D. Jorgensen, D.N. Argyriou, Phys. Rev. B 56 (1997) 8265.
[19] C.N.R. Rao, P.N. Santhosh, R.S. Singh, A. Arulraj, J. Solid State Chem. 135 (1998) 169.
[20] A.M. Balagurov, V.Y. Pomjakashin, D.V. Sheptyakov, V.L. Aksenov, P. Fisher, L. Keller, O.Y. Gorbenko, A.R. Kaul, N.A. Babuskina, Phys. Rev. B 64 (2001) 024420.
[21] J.P. Attfield, Cryst. Eng. 5 (2002) 427.
[22] L.M. Rodríguez Martínez, J.P. Attfield, Phys. Rev. B 54 (1996) R15622.
[23] L.M. Rodríguez Martínez, J.P. Attfield, Phys. Rev. B 63 (2000) 24424.
[24] J.P. Chapman, J.P. Attfield, L.M. Rodríguez Martínez, L. Lezama, T. Rojo, Dalton Trans. (2004) 3026.
[25] J.A. Collado, M.A.G. Aranda, C. Frontera, J.L. García-Muñoz, in preparation.
[26] R.D. Shannon, Acta Cryst. Sect. A 32 (1976) 751.
[27] A.C. Larson, R.B. Von Dreele, Los Alamos National Lab. Report No. LA-UR-86-748, 1994.
[28] G.K. Williamson, W.H. Hall, Acta Metall. 1 (1953) 22.
[29] P.M. Woodward, D.E. Cox, T. Vogt, C.N.R. Rao, A.K. Cheetham, Chem. Mater. 11 (1999) 3529.
[30] A. Llobet, C. Frontera, J.L. Garcia-Muñoz, C. Ritter, M.A.G. Aranda, Chem. Mater. 12 (2000) 3648.
[31] Y.B. Zhang, S. Li, C.Q. Sun, W. Gao, S.X. Dou, P. Hing, J. Appl. Phys. 90 (2001) 4583.
[32] A.P. Ramirez, P.E. Schiffer, S.-W. Cheong, C.H. Chen, W. Bao, T.T.M. Palstra, P.L. Gammel, D.J. Bishop, B. Zegarski, Phys. Rev. Lett. 76 (1996) 3188.
[33] A. Daoud-Aladine, J. Rodríguez-Carvajal, L. Pinsard-Gaudart, M.T. Fernández-Diaz, A. Revcolevschi, Phys. Rev. Lett. 89 (2002) 097205.